Effects of the nozzle exit section shape on the velocity field and heat transfer of impinging synthetic jets

G. Longobardo[1], G. Paolillo[1,*], T. Astarita[1], G. Cardone[1], C. S. Greco[1]

1: Dept. of Industrial Engineering, University of Naples "Federico II", Napoli, Italy
*Corresponding author: giosue.longobardo@unina.it

Keywords: synthetic jets, particle image velocimetry, infrared thermography.

ABSTRACT

The versatility and effectiveness of synthetic impinging jets for cooling applications have pushed the scientific community to optimize the design of such devices investigating the effects of all the relevant flow parameters, such as the stroke length, the Reynolds number and the shape of the driving wave. The current work focuses on the influence of different nozzle exit section shapes on the flow field evolution and heat transfer behavior of symthetic jets. In addition to the circular baseline case, three different shapes are comparatively assessed: the triangle, the square and the rectangular orifice. Simultaneous synchronized particle image velocimetry (PIV) and infrared thermography (IRT) measurements are made for three nozzle-to-plate distances: $H/D \in [2; 6; 10]$ whereas the Reynolds number and the Strouhal number are kept constant and equal to $Re = 3000$ and $St = 0.08$, respectively.

1. Introduction

Impinging jets find widespread application in various industrial processes requiring rapid cooling or heating, from internal cooling of aircraft engine turbine blades and combustor injectors to drying of paper and ceramic, as well as electronics cooling (Carlomagno & Ianiro, 2014). Within such a category, synthetic jets have garnered particular attention from the heat and mass transfer community for their advantageous features, such as the high reliability, the simplicity of design and the reduced sizes of their actuators (even suitable for micrometric applications) (Chaudhari et al., 2010; Valiorgue et al., 2009). A synthetic jet is generated by the periodic oscillation of an actuator (e.g., a diaphragm, a piezoelectric membrane or a piston) inside a cavity provided with an opening (generally an orifice or a nozzle). The periodic variation in cavity volume induces oscillations in cavity pressure, resulting in alternating phases of fluid ejection or suction across the opening. During the ejection phase, vortices form due to the flow separation at the exit of the orifice/nozzle, which then propagates downstream under their self-induced velocity. Therefore, a jet is "synthesized" from the ambient fluid without net mass flux across the opening. The behaviour of a synthetic jet

is essentially determined by two non-dimensional parameters: the Reynolds number $Re = U_0 D/\nu$ and the Strouhal number $St = fD/U_0$ where U_0 is a characteristic velocity scale, defined as in (1), D is the exit section diameter, ν the kinematic viscosity of air and f the operating frequency, τ and τ_e respectively represent the whole period of the synthetic jet and the period of the ejection phase alone, while U_e represents the exit velocity.

$$U_0 = \frac{1}{\tau} \int_0^{\tau_e} U_e(t) dt \tag{1}$$

In impinging configurations, another relevant parameter is the dimensionless impingement distance H/D, with H being the exit section-to-plate distance. In the literature, the effects of Re, St and H/D on both the velocity field structure and the heat transfer capabilities of impinging synthetic jets have been extensively investigated and quite good knowledge on this side has been gained (Greco et al., 2014, 2017). Part of the most recent research has also focused on the development of innovative configurations of synthetic jet devices for heat transfer enhancement and noise reduction. Several works have proven that a viable strategy in this direction is the modification of the orifice/nozzle shape. In their pioneering work, Chaudhari et al. (2010), observed that a square orifice is more effective than circular and rectangular shapes of $H/D > 5$ at the same flow conditions, whereas rectangular orifices achieve the best performance at smaller distances with an aspect ratio between 3 and 5. The later work of Bhapkar et al. (2014) demonstrated that even better heat transfer behaviour at short impingement distances might be obtained using elliptical shapes. On the other hand, Jeyalingam & Jabbal (2016) showed that, in comparison to circular orifices, lobed orifices offer a good broadband noise mitigation over the mid to high-frequency range.
The present study reports on the effects of the exit section shape on both the velocity fields and the heat transfer of impinging synthetic jets. The rectangular, triangular, square and circular orifices are tested for at different nozzle to plate distances: $H/D \in [2; 6; 10]$ for a Strouhal number equal to $St = 0.08$ and Reyndodls number equal to $Re = 3000$.

2. Experimental Setup

A summary of all the sub-components of the experimental setup is presented in figure 1. The setup has been designed to perform simultaneous synchronized particle image velocimetry (PIV) and infrared thermography (IRT) measurements. The following sub-sections will go into further details about the deployment of such experimental techniques. The setup presented herein is set to perform time-averaged as well as phase-averaged measurements, both for the IRT and the PIV setup. However only time-averaged results will be discussed in the present paper.

2.1. PIV Setup

The 2C-PIV setup is deployed as follows: stroboscopic illumination is provided by the Dantec Dynamics Dual Power Laser, a low-speed double pulsed Nd:YAG laser, emitting monochromatic coherent 532 nm light, 200 mJ maximum energy output and 15 Hz maximum operating frequency. Image pairs are acquired through an Andor Zyla sCMOS camera (2160 × 2560 pixels, pixel pitch of 6 μm, intensity resolution 16 bit) equipped with a standard Nikkor Nikon 50 mm lens with a maximum aperture of $f\#$ 1.8, set to $f\#$ 8 during the recording phase. The imaging setup produces a final FOV of about $10D \times 6D$, with a spatial resolution of about 11.5 px/mm. The flow is seeded with olive oil particles having a mean diameter of 1 μm and generated by a Laskin nozzle. Images are processed using PaIRS (Astarita & Cardone, 2005; Astarita, 2006, 2007, 2008, 2009) by means of a multi-pass multi-grid algorithm. The operating frequency of the laser is set using the following relation: $f_{laser} = \dfrac{f_{jet}}{1/N_{div.} + n}$, where f_{jet} is the characteristic frequency of the synthetic jet, N_{div} is the number of phases captured and n is the smallest integer that produces a laser operating frequency lower than the maximum laser repetition rate. Ensemble measurements are made using 600 images.

2.2. IRT Setup

An infrared camera (CEPID JADE III 320×240 InSb focal plane array) measures the foil surface temperature with a spatial resolution of 2.1 px/mm. The thermal camera is set to acquire images with a sampling frequency ten times higher than the operative frequency of the laser, while the integration time is fixed to 450 μs. A stainless steel foil (243 mm wide, 715 mm long and 40 μ m thick), constituting the target plate, is steadily and uniformly heated by Joule effect and it is cooled by the synthetic jets impinging on it. Two couples of bus bars, made of copper, clamped at the shortest sides of the foil are maintained at constant potential difference by using a stabilized DC power supply. Furthermore, the foil thermal expansion is balanced by the spring-loaded bolts linked to the bus bars and by two spring-loaded insulators. The foil surface is coated with high-emissivity paint ($\epsilon = 0.95$).

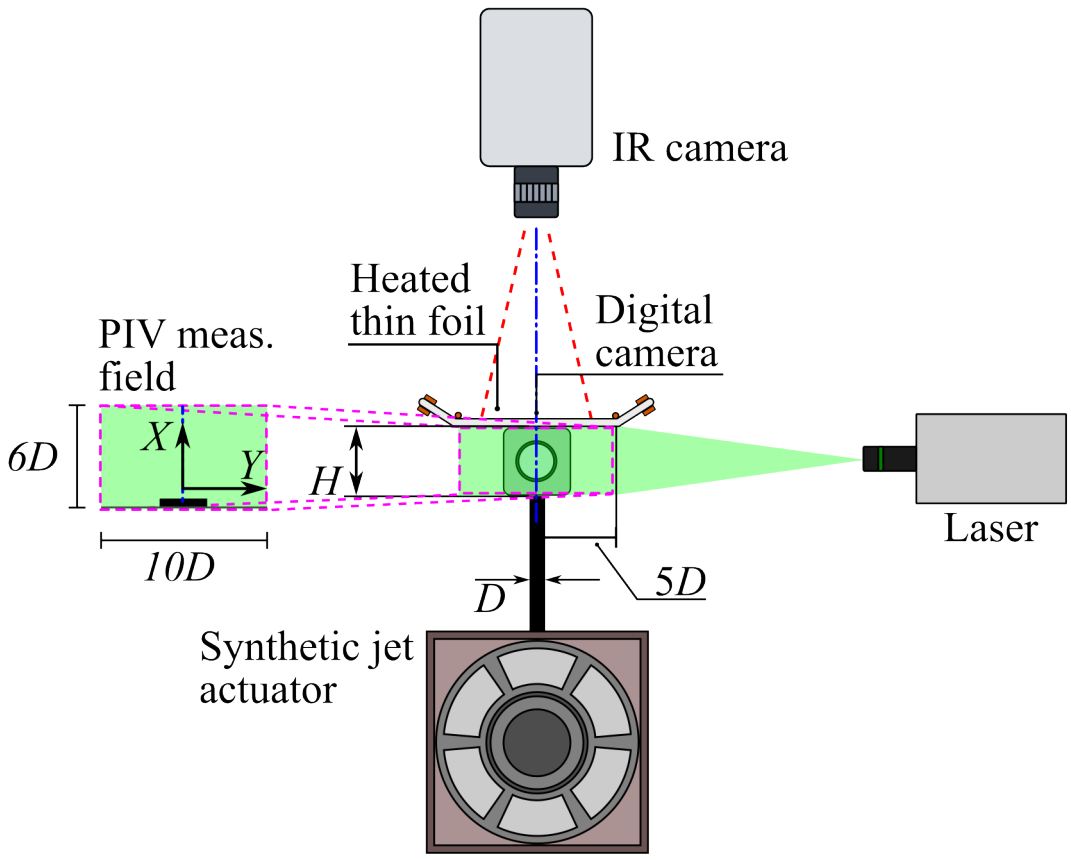

Figure 1. Schematics of the experimental setup.

2.3. Synthetic Jet Actuator

The synthetic jet is generated by a loudspeaker (CIARE HS250) with a diameter of 250 mm, oriented upward. Its nominal impedance is 16 Ω and its rated power is 160 W. The input signal provided to the loudspeaker is sinusoidal, with a frequency of 9 Hz. This signal is generated and managed by a USB oscilloscope and logic analyzer (Diligent Analog Discovery 2), before passing through a Hi-Fi amplifier (CIARE YSA 300). Four different nozzles have been tested, with different exit section shapes. Images shown in figure 2 compare the triangular, rectangular and square nozzle exit section shape with the circular one, which will be considered the baseline case. The reference configuration is a straight cylinder, with an inner diameter of 20 mm. The hydraulic diameter has been fixed among the different geometries. The hydraulic diameter is defined as in the following equation: $D_i = 4S/p$, where S is the area of the orifice and p is its perimeter. By defining the Reynolds number via the hydraulic diameter, D_i, it is possible to set the same operating frequency of the loudspeaker for every nozzle, provided that the effective velocity at the exit section is kept constant. The target exit velocity is $U_0 = 2.25$ m/s, which outputs a Reynolds number of about $Re = 3000$. However, by keeping the hydraulic diameter constant among different geometries, the exit sectional areas are different for every geometry, clearly visible in figure 2. In turn,

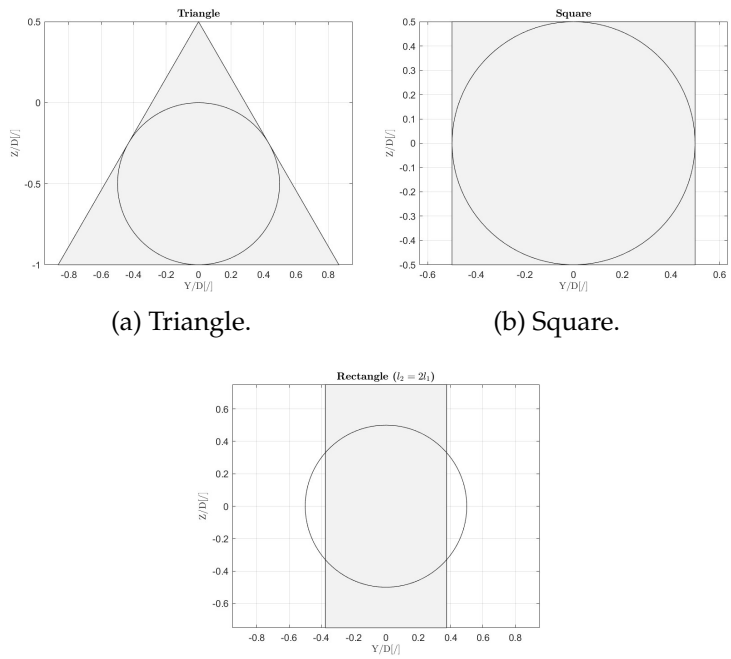

(a) Triangle.

(b) Square.

(c) Rectangle ($l_2 = 2l_1$).

Figure 2. A comparison between the circular section (solid black line) and the different exit sections (shaded grey areas).

different exit sectional areas produce different exit velocities for a given amplitude of the sinusoidal wave driving the loudspeaker. Indeed a nozzle characterization procedure was performed through hot-wire anemometry via the MiniCTA 54T42 fitted with a 55P11 probe, both from Dantec Dynamics: the amplitude of the sinusoidal wave was tuned to a measured output velocity of each nozzle equal to $U_0 = 2.25$ m/s.

3. Results

The following measurements comprise time-averaged flow fields and time-averaged Nusselt number maps performed for all the different nozzle exit section shapes (NESSs) at three different nozzle-to-plate distances $H/D \in [2; 6; 10]$ and Strouhal number equal to $St = 0.08$. In the following sub-sections data will be presented for all the different test cases, and, for the sake of brevity, different nozzle exit section shapes will be indicated with the following notation: C for the circular baseline case, T for the triangular nozzle, S for the square nozzle, R for the rectangular nozzle. In all of the following PIV velocity contours, the nozzle (when present within the field of view) and the impinged plate are indicated by a black patch while a shaded black region is placed in correspondence of the area not illuminated by the laser. Images shown in figures 3-6 show a side-by-side comparison of the PIV time-averaged vertical velocity contour with 2D streamlines superimposed and the Nusselt number map obtained through IRT measurements. As expected, for every case, the higher the nozzle-to-plate distance, the wider the jet spreads across the field of view. Similarly, high nozzle-to-plate distance is also associated with a high reduction in vertical velocity in the proximity of the impinged plate. On the contrary, for the small nozzle-to-plate distances, the stagnation zone is smaller, especially for $H/D = 2$. This behavior is also confirmed by the corresponding Nusselt number map, where the thermal pattern is more spread across the plate as well. For the sake of clarity, these measurements are presented as comparison between the baseline case geometry, the circular nozzle, and the other nozzle shapes, for this reason the Nusselt contours and the vertical velocity maps are shown with a colormap that shares the same limits for every case. A distinctive behavior can be seen in the time-averaged vertical velocity map for the rectangular nozzle: for the largest nozzle to plate distance, $H/D = 10$, the jet shows a significantly higher spreading. It is to be noted that the rectangular nozzle exit section shape is the only one having a clear preferential direction since $l_2 = 2l_1$, and the major axis of the nozzle is aligned with the major axis of the plate, along the Y direction. Such enhanced spreading can be seen from $X/D = 3$, in figure 6 (c). The smaller nozzle-to-plate distances also exhibit a pattern resembling the nozzle exit section shape, while whenever the nozzle is placed further from the plate, such footprint in the Nu pattern is lost and all patterns revert to a circular-like shape.

3.1. $NESS = C$, $St = 0.08$

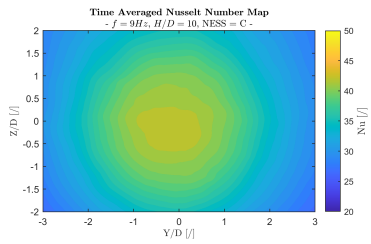

(a) Nu map, $H/D = 10$.

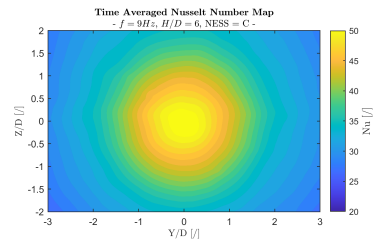

(b) Nu map, $H/D = 6$.

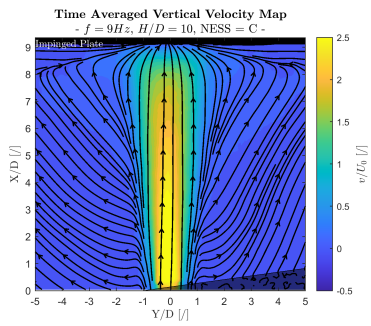

(c) v map, $H/D = 10$.

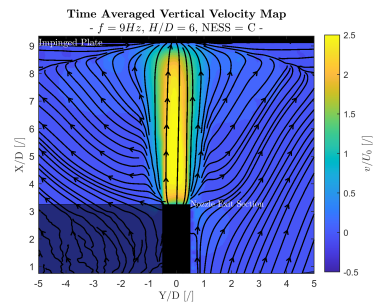

(d) v map, $H/D = 6$.

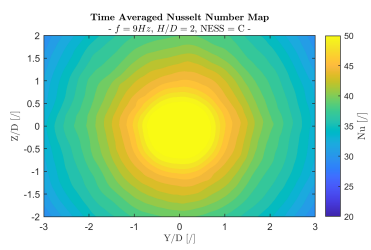

(e) Nu map, $H/D = 2$.

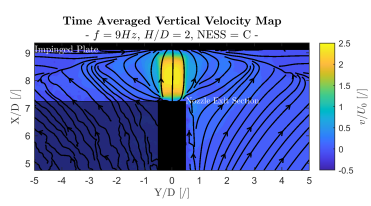

(f) v map, $H/D = 2$.

Figure 3. Nu and v maps for different nozzle-to-plate distances, $NESS = C$.

3.2. $NESS = T$, $St = 0.08$

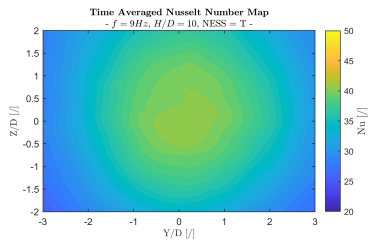

(a) Nu map, $H/D = 10$.

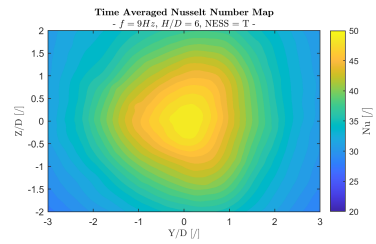

(b) Nu map, $H/D = 6$.

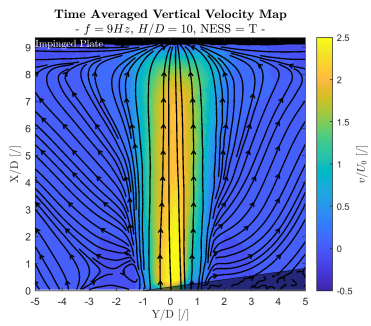

(c) v map, $H/D = 10$.

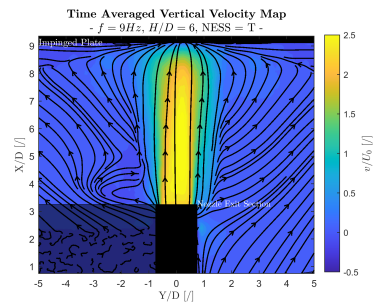

(d) v map, $H/D = 6$.

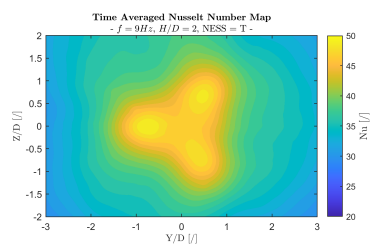

(e) Nu map, $H/D = 2$.

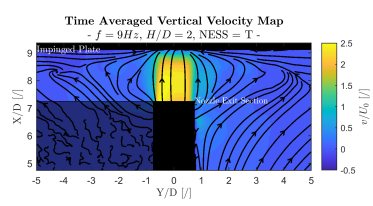

(f) v map, $H/D = 2$.

Figure 4. Nu and v maps for different nozzle-to-plate distances, $NESS = T$.

3.3. $NESS = S$, $St = 0.08$

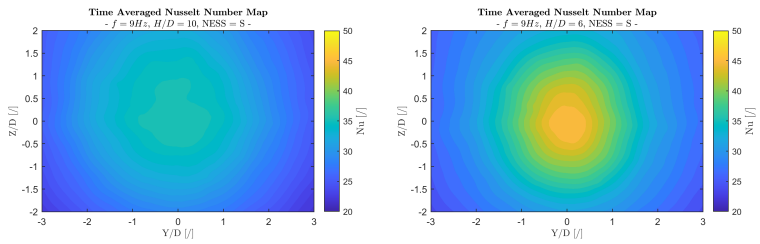

(a) Nu map, $H/D = 10$.

(b) Nu map, $H/D = 6$.

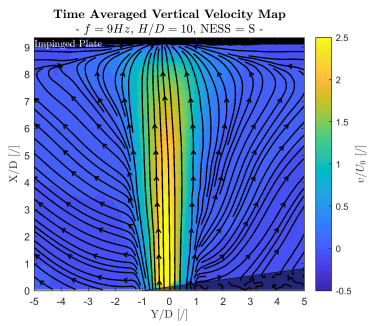

(c) v map, $H/D = 10$.

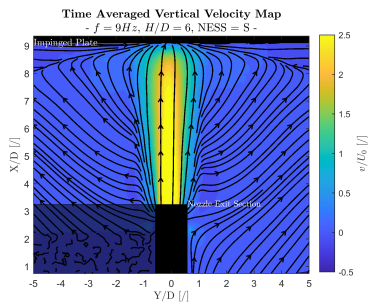

(d) v map, $H/D = 6$.

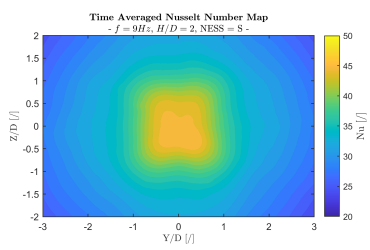

(e) Nu map, $H/D = 2$.

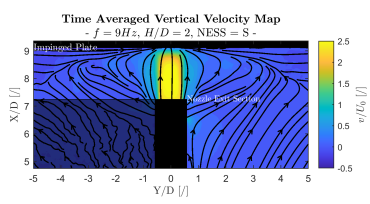

(f) v map, $H/D = 2$.

Figure 5. Nu and v maps for different nozzle-to-plate distances, $NESS = S$.

3.4. $NESS = R$, $St = 0.08$

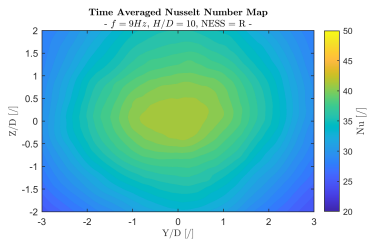

(a) Nu map, $H/D = 10$.

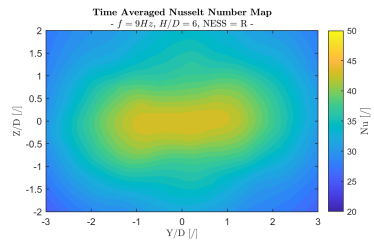

(b) Nu map, $H/D = 6$.

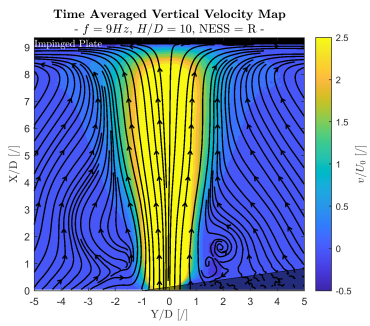

(c) v map, $H/D = 10$.

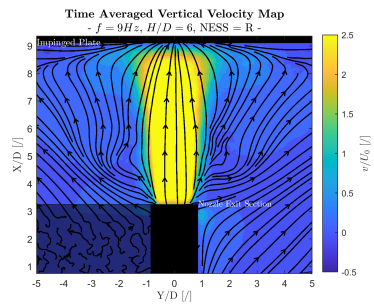

(d) v map, $H/D = 6$.

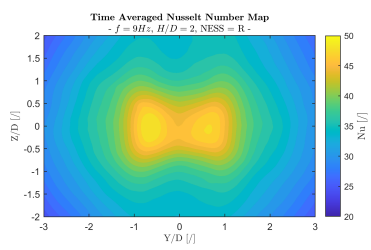

(e) Nu map, $H/D = 2$.

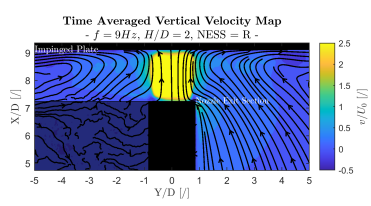

(f) v map, $H/D = 2$.

Figure 6. Nu and v maps for different nozzle-to-plate distances, $NESS = R$.

4. Conclusions

Preliminary measurements are performed to investigate the effect of the nozzle exit section shape on both the flow field and the heat transfer capabilities of a synthetic jet by means of simultaneous synchronized 2C-PIV and IRT measurement. Consistent results are found both in terms of flow fields as well as Nusselt patterns: small nozzle-to-plate distances exhibit less spreading of the jet combined with a less spreaded, although more intense, Nu pattern. Smaller nozzle-to-plate distances also reveal the shape of the nozzle in the thermal pattern: this behavior can be seen for every nozzle and it is associated with the presence of a Nu peak in correspondence of every corner of the shape. Larger nozzle-to-plate distances are associated with a higher spreading in the jet and a lower vertical velocity in the vicinity of the impinged plate. A peculiar behavior in the time-averaged vertical velocity map can be observed for the rectangular shape: the jet exhibits a significantly higher spreading in its major axis, which is aligned with the plate's major axis from $X/D = 3$ and upwards. Future work will focus on the characterization of the phase-averaged flow fields and Nusselt number maps to provide a clearer overview of the underlying physics by analyzing the evolution in time of the phenomenon.

Nomenclature

Re	Reynolds number [/]
St	Strouhal number [/]
Nu	Nusselt number [/]
H	Nozzle-to-plate distance [m]
D	Nozzle diameter [m]
D_i	Hydraulic diameter [m]
L_0	Stroke length [m]
f	Operating frequency [Hz]
U_0	Velocity scale [m/s]
ν	Kinematic viscosity [m/s2]
v, u	Vertical and horizontal velocity components [m/s]
X, Y, Z	Coordinate axis reference system

References

Astarita, T. (2006, 06). Analysis of interpolation schemes for image deformation methods in piv: Effect of noise on the accuracy and spatial resolution. *Experiments in Fluids*, *40*, 977-987. doi:

10.1007/s00348-006-0139-4

Astarita, T. (2007, 11). Analysis of weighting windows for image deformation methods in piv. *Experiments in Fluids*, *43*, 859-872. doi: 10.1007/s00348-007-0314-2

Astarita, T. (2008, 08). Analysis of velocity interpolation schemes for image deformation methods in piv. *Experiments in Fluids*, *45*, 257-266. doi: 10.1007/s00348-008-0475-7

Astarita, T. (2009, 06). Adaptive space resolution for piv. *Experiments in Fluids*, *46*, 1115-1123. doi: 10.1007/s00348-009-0618-5

Astarita, T., & Cardone, G. (2005, 02). Analysis of interpolation schemes for image deformation methods in piv. *Experiments in Fluids*, *38*, 233-243. doi: 10.1007/s00348-004-0902-3

Bhapkar, U. S., Srivastava, A., & Agrawal, A. (2014). Acoustic and heat transfer characteristics of an impinging elliptical synthetic jet generated by acoustic actuator. *International Journal of Heat and Mass Transfer*, *79*, 12-23. doi: https://doi.org/10.1016/j.ijheatmasstransfer.2014.07.083

Carlomagno, G. M., & Ianiro, A. (2014). Thermo-fluid-dynamics of submerged jets impinging at short nozzle-to-plate distance: A review. *Experimental Thermal and Fluid Science*, *58*, 15-35. doi: https://doi.org/10.1016/j.expthermflusci.2014.06.010

Chaudhari, M., Puranik, B., & Agrawal, A. (2010). Heat transfer characteristics of synthetic jet impingement cooling. *International Journal of Heat and Mass Transfer*, *53*(5), 1057-1069. doi: https://doi.org/10.1016/j.ijheatmasstransfer.2009.11.005

Greco, C. S., Cardone, G., & Soria, J. (2017). On the behaviour of impinging zero-net-mass-flux jets. *Journal of Fluid Mechanics*, *810*, 25–59. doi: 10.1017/jfm.2016.703

Greco, C. S., Ianiro, A., & Cardone, G. (2014). Time and phase average heat transfer in single and twin circular synthetic impinging air jets. *International Journal of Heat and Mass Transfer*, *73*, 776-788. doi: https://doi.org/10.1016/j.ijheatmasstransfer.2014.02.030

Jeyalingam, J., & Jabbal, M. (2016, 06). Optimization of synthetic jet actuator design for noise reduction and velocity enhancement.. doi: 10.2514/6.2016-4236

Valiorgue, P., Persoons, T., McGuinn, A., & Murray, D. (2009). Heat transfer mechanisms in an impinging synthetic jet for a small jet-to-surface spacing. *Experimental Thermal and Fluid Science*, *33*(4), 597-603. doi: https://doi.org/10.1016/j.expthermflusci.2008.12.006